EVS35 Symposium
Oslo, Norway, June 11-15, 2022

A Physics-based Electrode-level Thermal Model for Advanced Battery Management

Aloisio Kawakita de Souza[1,2], Gregory L. Plett[1,3], M. Scott Trimboli[1,4]
[1]*Department of Electrical and Computer Engineering, University of Colorado Colorado Springs, Colorado Springs, CO 80918, United States*
[2]akawakit@uccs.edu, [3]gplett@uccs.edu, [4]mtrimbol@uccs.edu

Summary

Electric-vehicle lithium-ion battery packs require careful monitoring to ensure safe and reliable performance. State-of-the-art battery management systems (BMS) rely on highly accurate battery models for the timely parameter estimates needed during operation. In addition to electrochemical dynamics, a battery's thermal behavior introduces critical limits on battery performance and lifetime. This paper presents a physics-based development for a first-principles mathematical model of lithium-ion battery thermal dynamics that can be used in state estimation and advance control schemes in on-board BMS applications.

1 Abstract

High-performance energy-storage systems for BEVs must operate close to operational limits to maximize effectiveness and optimize energy utilization. Such boundary-following behavior, however, increases the need for careful monitoring of a battery's internal state to ensure safe and reliable operation.
Physics-based mathematical representations of electrochemical dynamics have emerged as the model of choice as they allow estimation of key internal variables that serve as true indicators of battery health and can be used to inform advanced control strategies that mitigate premature cell aging. The electrochemical pseudo two-dimensional (P2D) model is widely accepted as a faithful mathematical depiction of true lithium-ion cell-level behavior. Nonetheless, this model fails to account for the crucially important effect of internal heat generation. To that end, we introduce a mathematical model of heat generation that is purely physics-based and is described at the electrode-level to enforce consistency with the physics-based electrochemical model. Both models feature a "lumped-parameter" approach that packages the model descriptors in an efficient manner as required by nondestructive parameter identification methods. In addition, we develop a reduced-order model framework to enable efficient computation of physics-based estimates of cell states for use in advanced controls.
The initial P2D model was introduced in [1] and is known as the Doyle Fuller Newman (DFN) model after its inventors; a full account can be found in [2]. Numerous refinements of the DFN have appeared in the literature, including the addition of double layer effects [3].
It is important to note that the classic DFN model is not strictly identifiable; i.e., it is not mathematically possible to discern the full set of internal variables from measurements of input-output data. To that end, the work of [4] and others have given rise to a lumped parameter model (LPM) whereby the classic parameter set is condensed to a fully identifiable set. The LPM version of the DFN model will serve as

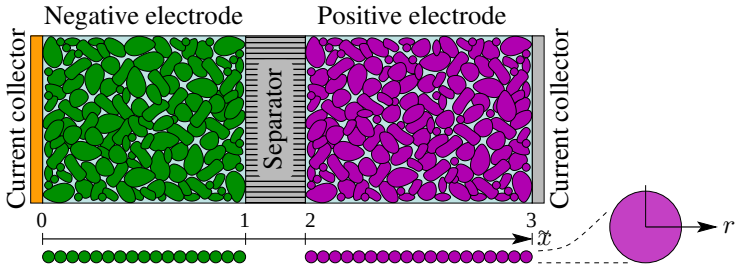

Figure 1: Illustration of the cross-sectional geometry of a lithium-ion cell.

the fundamental electrochemical framework upon which the present physics-based thermal model will be developed.

2 Physics-based coupled electrochemical-thermal model

The physics-based coupled electrochemical-thermal model (PBCET) presented in this work comprises a lumped-parameter version of the P2D model coupled to a simple lumped thermal model. The coupling between the two models is manifest through two distinct mechanisms: 1) heat generated within the electrodes and separator (due to the electrochemical reactions during dis-/charging); and 2) temperature-dependency of the P2D model parameters and reactions. The following section summarizes the model.

2.1 Lumped-parameter P2D model

The P2D model, first introduced in [1,5], comprises a set of four partial differential equations (PDEs) that describe mass and charge conservation within a cell, and one algebraic closure term that captures reaction kinetics at the active porous structure of both electrodes during de-intercalation/intercalation of lithium ions. Although this model is widely adopted in the literature, its computational complexity and challenging parameterization are key limiting factors to widespread adoption in next-generation physics-based BMS. In order to achieve a trade-off between accuracy and computational complexity, various simplified versions of the P2D model have been proposed. Nonetheless, parameterization of these simplified models still remains a challenge because of the large number of parameters that must be identified, and the fact that some parameterizations are not identifiable. To overcome this limitation, a lumped-parameter reformulation of the P2D model was proposed in [3], which creates pseudo-dimensionless variables by normalizing the length scales and lumping together parameters that appear in groups. Recent work [6], leverages the lumped-parameter model (LPM) from [3], to develop a method for converting the classic DFN model to a fully identifiable LPM . We adopt this LPM in the present work due to its suitability for model parameterization using non-destructive means, namely, relying solely on experimental input/output data. We present important highlights of the LPM model in what follows.
Fig. 1 illustrates the geometry of a 1-d slice through a lithium-ion cell; the electrode thickness dimension is normalized according to [3, 6], yielding corresponding values of $\tilde{x}$ within each cell region:

$$0 \leq \tilde{x} \leq 1 \text{ negative electrode,}$$

$$1 \leq \tilde{x} \leq 2 \text{ separator region,}$$

$$2 \leq \tilde{x} \leq 3 \text{ positive electrode.}$$

The lumped-parameter P2D model describes the following physical variables as functions of spatial location $\tilde{x}$ and time t:

- $\theta_{\mathrm{s}}^{\mathrm{r}}(\tilde{x}, r, t)$ Concentration of lithium in the solid electrode particles [unitless].
- $\theta_{\mathrm{ss}}^{\mathrm{r}}(\tilde{x}, t)$ Concentration in the particles at the particle/electrolyte boundary [unitless].
- $\theta_{\mathrm{e}}^{\mathrm{r}}(\tilde{x}, t)$ Concentration of lithium in the electrolyte [unitless].
- $\phi_{\mathrm{s}}^{\mathrm{r}}(\tilde{x}, t)$ Potential in the solid electrode particles [volts].
- $\phi_{\mathrm{s}}^{\mathrm{r}}(\tilde{x}, t)$ Potential in the electrolyte [volts].
- $\dot{n}^{\mathrm{r}}(\tilde{x}, t)$ Lithium flux from solid electrode particles into the electrolyte $[\mathrm{mol\,s^{-1}}]$.

Note that superscript $\mathrm{r} \in \{\mathrm{n},\ \mathrm{s},\ \mathrm{p}\}$ denotes "region" where "n" is negative electrode, "s" is separator and

"p" is positive electrode. We now review the five first-principles equations governing the electrochemical dynamics.

EQUATION I: CHARGE CONSERVATION IN THE SOLID. Charge conservation in the porous electrode structure is modeled by Ohm's law and measured in volts. The lumped-parameter PDE for charge conservation in both negative- positive-electrodes is given as,

$$\bar{\sigma}^{\mathrm{r}} \frac{\partial^2 \phi_{\mathrm{s}}^{\mathrm{r}}}{\partial \tilde{x}^2} = F \dot{n}^{\mathrm{r}},$$

where $\bar{\sigma}^{\mathrm{r}}$ is the lumped effective conductivity of the electrode and measured in siemens. On the right side, F is the Faraday constant. The initial values are given by,

$$\phi_{\mathrm{s},0}^{\mathrm{n}} = 0$$
$$\phi_{\mathrm{s},0}^{\mathrm{p}} = U_{\mathrm{ocp}}^{\mathrm{p}}(\theta_{\mathrm{s},0}^{\mathrm{p}}) - U_{\mathrm{ocp}}^{\mathrm{n}}(\theta_{\mathrm{s},0}^{\mathrm{n}})$$

where $\theta_{\mathrm{s}}^{\mathrm{r}} = c_{\mathrm{s}}^{\mathrm{r}}/c_{\mathrm{s,max}}^{\mathrm{r}}$ is the non-dimensional stoichiometry and where $\theta_{\mathrm{s},0}^{\mathrm{r}} = c_{\mathrm{s},0}^{\mathrm{r}}/c_{\mathrm{s,max}}^{\mathrm{r}}$ is the initial equilibrium of the electrode; $U_{\mathrm{ocp}}^{\mathrm{r}}(\theta_{\mathrm{s}}^{\mathrm{r}})$ is the open-circuit potential (OCP) of the electrode as a function of local stoichiometry. The nonzero boundary conditions are

$$\bar{\sigma}^{\mathrm{n}} \frac{\partial \phi_{\mathrm{s}}^{\mathrm{n}}}{\partial \tilde{x}}\bigg|_{\tilde{x}=0} = \bar{\sigma}^{\mathrm{p}} \frac{\partial \phi_{\mathrm{s}}^{\mathrm{p}}}{\partial \tilde{x}}\bigg|_{\tilde{x}=3} = -i_{\mathrm{app}}.$$

EQUATION II: MASS CONSERVATION IN THE SOLID. Mass conservation in the spherical active porous materials is modeled by Fick's law of diffusion. It is valid for both negative- and positive-electrode regions and is described by the following lumped-parameter PDE,

$$\frac{\partial \theta_{\mathrm{s}}^{\mathrm{r}}}{\partial t} = \frac{1}{\tilde{r}^2} \frac{\partial}{\partial \tilde{r}} \left(\bar{D}_{\mathrm{s}}^{\mathrm{r}} \tilde{r}^2 \frac{\partial \theta_{\mathrm{s}}^{\mathrm{r}}}{\partial \tilde{r}} \right)$$

where $\bar{D}_{\mathrm{s}}$ is the lumped diffusion coefficient with units s^{-1}. The non-dimensional radial coordinate inside the spherical particle is represented by $\tilde{r}$. The initial value and nonzero boundary condition are given by,

$$\breve{c}_{\mathrm{s},0}^{\mathrm{r}} = \frac{10\,800 \bar{D}_{\mathrm{s}}^{\mathrm{r}} Q}{F\,|\theta_{100}^{\mathrm{r}} - \theta_0^{\mathrm{r}}|} \left(\theta_0^{\mathrm{r}} + z_0(\theta_{100}^{\mathrm{r}} - \theta_0^{\mathrm{r}})\right)$$
$$\frac{\partial \breve{c}_{\mathrm{s}}^{\mathrm{r}}}{\partial \tilde{r}}\bigg|_{\tilde{r}=1} = -F \dot{n}^{\mathrm{r}},$$

respectively. The initial cell state of charge is given by z_0 where $0 \leq z_0 \leq 1$. The initial electrode stoichiometry, θ_0^{r}, is the value of $\theta_{\mathrm{s}}^{\mathrm{r}}$ when the cell is resting at $0\,\%$ SOC; $\theta_{100}^{\mathrm{r}}$ is the value of $\theta_{\mathrm{s}}^{\mathrm{r}}$ when the cell is resting at $100\,\%$ SOC.

EQUATION III: CHARGE CONSERVATION IN THE ELECTROLYTE. Charge conservation in the electrolyte is based on the principle that the net quantity of electric charge is always conserved in an isolated system. Therefore, the charge conservation in the electrolyte is modeled by the following lumped-parameter PDE,

$$\frac{\partial}{\partial \bar{x}} \left(\bar{\kappa}^{\mathrm{r}} \left(\frac{\partial}{\partial \tilde{x}} \phi_{\mathrm{e}}^{\mathrm{r}} + \bar{\kappa}_D T \frac{\partial \ln(\theta_{\mathrm{e}}^{\mathrm{r}})}{\partial \tilde{x}} \right) \right) + F \dot{n}^{\mathrm{r}} = 0$$

where $\bar{\kappa}^{\mathrm{r}}$ is the lumped effective conductivity of the electrolyte. The nonzero boundary conditions are given by,

$$\bar{\kappa}^{\mathrm{r}} \left[\frac{\partial}{\partial \tilde{x}} \phi_{\mathrm{e}}^{\mathrm{r}} - T \bar{\kappa}_D \frac{\partial \ln(\theta_{\mathrm{e}}^{\mathrm{r}})}{\partial \tilde{x}} \right]\bigg|_{\tilde{x}=1,2} = -i_{\mathrm{app}}.$$

EQUATION IV: MASS CONSERVATION IN THE ELECTROLYTE. Mass conservation in the electrolyte models the linear diffusion of lithium in the electrolyte and the local resistance to the flux of lithium from the porous electrode structure into the electrolyte. The lumped-parameter PDE is given as follows,

$$\bar{n}_{\mathrm{e}}^{\mathrm{r}} \frac{\partial \theta_{\mathrm{e}}^{\mathrm{r}}}{\partial t} = \bar{\psi} \frac{\partial}{\partial \tilde{x}} \bar{\kappa}^{\mathrm{r}} \frac{\partial}{\partial \tilde{x}} \theta_{\mathrm{e}}^{\mathrm{r}} + \dot{n}^{\mathrm{r}}$$

where $\bar{n}_{\mathrm{e}}^{\mathrm{r}}$ is measured in mol, $\bar{\psi}$ in $\mathrm{mol\,S^{-1}\,s^{-1}}$ and $\bar{\kappa}^{\mathrm{r}}$ in S. The initial value is $\theta_{\mathrm{e},0} = 1$ and the nonzero boundary conditions are as follows:

$$\bar{\kappa}^{\mathrm{n}} \frac{\partial}{\partial \tilde{x}} \theta_{\mathrm{e}}^{\mathrm{n}}\bigg|_{\tilde{x}=1^-} = \bar{\kappa}^{\mathrm{s}} \frac{\partial}{\partial \tilde{x}} \theta_{\mathrm{e}}^{\mathrm{s}}\bigg|_{\tilde{x}=1^+}, \qquad \text{negative-electrode/separator interface,}$$

$$\bar{\kappa}^{\mathrm{s}} \frac{\partial}{\partial \tilde{x}} \theta_{\mathrm{e}}^{\mathrm{s}} \Big|_{\tilde{x}=2^-} = \bar{\kappa}^{\mathrm{p}} \frac{\partial}{\partial \tilde{x}} \theta_{\mathrm{e}}^{\mathrm{p}} \Big|_{\tilde{x}=2^+}, \qquad \text{separator/positive-electrode interface.}$$

The continuity boundary conditions at the electrode/separator boundaries are:

$$\theta_{\mathrm{e}}^{\mathrm{n}}|_{\tilde{x}=1^-} = \theta_{\mathrm{e}}^{\mathrm{s}}|_{\tilde{x}=1^+}, \quad \text{and} \quad \theta_{\mathrm{e}}^{\mathrm{s}}|_{\tilde{x}=2^-} = \theta_{\mathrm{e}}^{\mathrm{p}}|_{\tilde{x}=2^+}.$$

EQUATION V: KINETICS. Electrochemical kinetics are modeled by the Butler–Volmer equation, which describes the dependency of the electrode electrical current on the electrode potential. Therefore, the lumped molar flux equation in the negative- and positive-electrode is given by

$$\begin{aligned}
\dot{n}^{\mathrm{r}} &= \dot{n}_0^{\mathrm{r}} \left(\exp\left(\tfrac{(1-\alpha^{\mathrm{r}})F}{RT} \eta^{\mathrm{r}} \right) - \exp\left(\tfrac{-\alpha^{\mathrm{r}} F}{RT} \eta^{\mathrm{r}} \right) \right) \\
\dot{n}_0^{\mathrm{r}} &= \bar{k}_0^{\mathrm{r}} \left(\theta_{\mathrm{e}}^{\mathrm{r}}\right)^{1-\alpha^{\mathrm{r}}} \left(1-\theta_{\mathrm{ss}}^{\mathrm{r}}\right)^{1-\alpha^{\mathrm{r}}} \left(\theta_{\mathrm{ss}}^{\mathrm{r}}\right)^{\alpha^{\mathrm{r}}} \\
\eta^{\mathrm{r}} &= \phi_{\mathrm{s}}^{\mathrm{r}} - \phi_{\mathrm{e}}^{\mathrm{r}} - U_{\mathrm{ocp}}^{\mathrm{r}}\left(\theta_{\mathrm{ss}}^{\mathrm{r}}\right) - F \bar{R}_{\mathrm{f}}^{\mathrm{r}} \dot{n}^{\mathrm{r}}
\end{aligned}$$

where $\dot{n}_0^{\mathrm{r}}$ is the lumped exchange current density in $\mathrm{mol\,s^{-1}}$, η^{r} is the local overpotential in volts, α^{r} is the charge-transfer coefficient, $\bar{k}_0^{\mathrm{r}}$ is a lumped reaction-rate constant in $\mathrm{mol\,s^{-1}}$, and $\bar{R}_{\mathrm{f}}^{\mathrm{r}}$ is the lumped resistivity of the surface film in ohms.

2.2 Thermal model

Augmenting the LPM with a physics-based thermal model makes it possible to influence battery performance by accurately informing advanced control algorithms of the internal electrochemical state and temperature. In order to effect a compromise between model accuracy and computational cost for on-board BMS applications, we prefer a lumped thermal model that is computationally light and relatively easy to parameterize. The simplified lumped thermal model adopted in this work is adopted from [7], and models the temperature evolution of the battery core and surface caused by the internal heat generated during dis/charge processes. Moreover, the model makes the further simplifying assumptions that the internal and surface temperatures are uniform and the heat generation is uniformly distributed within the battery jelly roll. The simplified lumped thermal model is described as follows:

$$C_1 \frac{dT_{in}}{dt} = \bar{q} - \lambda_1 \left(T_{in} - T_{sh}\right) \tag{1}$$

$$C_2 \frac{dT_{sh}}{dt} = k_1 \left(T_{in} - T_{sh}\right) - k_2 \left(T_{sh} - T_c\right), \tag{2}$$

where T_{in}, T_s and T_c are the internal, surface and cooling temperatures expressed in Kelvin (K), respectively; $\bar{q}$ is the total heat generation in Watts and the overbar notation indicates an average quantity. Constants C_1 and C_2 are the battery internal and surface heat capacities, respectively; λ_1 is the heat conduction coefficient between the battery core and the surface; and λ_2 is the heat conduction coefficient between the battery surface and the ambient environment. Since our interest is in an embedded processing BMS application, we shall convert our expressions into a discrete-time setting. Upon discretizing Eqs. 1 and 2, we may write the lumped thermal model in state-space form as:

$$\begin{bmatrix} T_{in}[k+1] \\ T_{sh}[k+1] \end{bmatrix} = \begin{bmatrix} \left(1 - \frac{\lambda_1 \Delta t}{C_1}\right) & \frac{\lambda_1 \Delta t}{C_1} \\ \frac{\lambda_1 \Delta t}{C_2} & \left(1 - \frac{\lambda_1 \Delta t}{C_2} - \frac{\lambda_2 \Delta t}{C_2}\right) \end{bmatrix} \begin{bmatrix} T_{in}[k] \\ T_{sh}[k] \end{bmatrix} + \begin{bmatrix} \frac{\Delta t}{C_1} & 0 \\ 0 & \frac{\lambda_2 \Delta t}{C_2} \end{bmatrix} \begin{bmatrix} \bar{q}[k] \\ T_f[k] \end{bmatrix} \tag{3}$$

where Δt is the sampling period in seconds.

2.2.1 Heat generation coupling

The total heat generation rate in each cell region is the sum of the average of the reversible, irreversible and ohmic heat generation rate terms, and is written as

$$\bar{q}^{\mathrm{r}} = \bar{q}_i^{\mathrm{r}} + \bar{q}_r^{\mathrm{r}} + \bar{q}_e^{\mathrm{r}} + \bar{q}_s^{\mathrm{r}} + \bar{q}_c^{\mathrm{r}},$$

where again, $\mathrm{r} \in \{\mathrm{n}, \mathrm{s}, \mathrm{p}\}$. In this expression, q_i is the irreversible heat generation due to chemical reactions at the interface; q_r is the reversible heat of entropy change; q_e is joule heating originating from the electrical potential gradient in the electrolyte; q_s is the joule heating from the electrical potential gradient in the solid; and q_c is the joule heating due to the contact resistance. The individual heat generation terms are obtained by converting the heat generation model developed in [8] to a lumped-parameter model using the approach presented in [6] and are derived as follows.

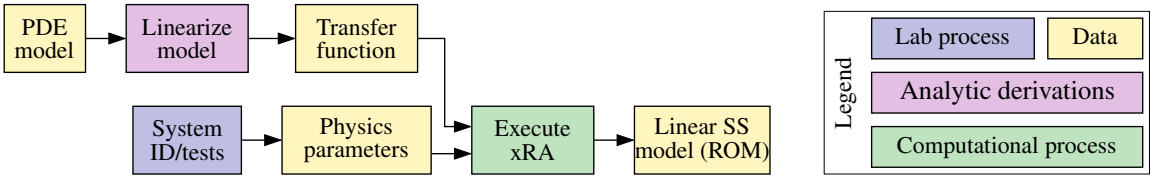

Figure 2: ROM generation process.

The irrerversible heat generation due to de-/intercalation of lithium is written in the lumped-parameter form as

$$q_{\mathrm{i}} = \dot{n}^{\mathrm{r}} \eta^{\mathrm{r}}, \tag{4}$$

where $\mathrm{r} \in \{\mathrm{n}, \mathrm{p}\}$. The reversible heat generation due to a change in entropy during de-/intercalation is

$$q_{\mathrm{r}} = \dot{n}^{\mathrm{r}} T \frac{\partial U_{\mathrm{ocp}}}{\partial T}, \tag{5}$$

where $\mathrm{r} \in \{\mathrm{n}, \mathrm{p}\}$ and $\frac{\partial U_{\mathrm{ocp}}}{\partial T}$ is the partial molar entropy term that relates changes in U_{ocp} with respect to temperature. The heat generation due to polarization caused by the ionic resistance of the electrolyte is written as

$$q_{\mathrm{e}} = \bar{\kappa}^{\mathrm{r}} \left(\nabla \phi_{\mathrm{e}}^{\mathrm{r}} \cdot \nabla \phi_{\mathrm{e}}^{\mathrm{r}} \right) + \bar{\kappa}^{\mathrm{r}} \bar{\kappa}_D T \left(\nabla \ln \theta_{\mathrm{e}}^{\mathrm{r}} \cdot \nabla \phi_{\mathrm{e}}^{\mathrm{r}} \right), \tag{6}$$

where $\mathrm{r} \in \{\mathrm{n}, \mathrm{s}, \mathrm{p}\}$, and the heat generation due to polarization of the electronic resistance of the solid material is written as

$$q_{\mathrm{s}} = \bar{\sigma}^{\mathrm{r}} \left(\nabla \phi_{\mathrm{s}}^{\mathrm{r}} \cdot \nabla \phi_{\mathrm{s}}^{\mathrm{r}} \right). \tag{7}$$

Finally, the heat generation due to polarization caused by the contact resistance between the current collectors and active material is written as

$$q_{\mathrm{c}} = R_{\mathrm{c}} i_{\mathrm{app}}^2,$$

where R_{c} is the contact resistance.

2.2.2 Thermal coupling and Arrhenius' law

The physico-chemical model parameters such as the solid diffusivity coefficient, electrolyte conductivity, and electrolyte diffusivity are all highly dependent on cell temperature. The temperature-dependency of the model parameters may be described by an Arrhenius' law temperature-dependency, written as [9]

$$\psi = \psi^{\mathrm{ref}} \exp \left[\frac{E_a^{\psi}}{R} \left(\frac{1}{T^{\mathrm{ref}}} - \frac{1}{T} \right) \right]$$

where ψ is a generic model parameter and ψ^{ref} is the value of this parameter at T^{ref}; E_a^{ψ} is the corresponding energy of activation for parameter ψ.

3 Physics-based reduced-order model

The PBCET model presented in Section 2 comprises a set of coupled PDEs that can only be solved numerically using specialized software and is computationally intensive. Consequently, the equations as given are not suitable for real-time embedded BMS applications. Alternatively, we seek a means to reduce the overall dimension of the problem so that it can (i) be solved with modest computational effort, and (ii) retain important physics-based information contained in the full-order PBM. To that end, we adopt a model-order reduction approach [10] that converts transcendental transfer functions (TFs) (obtained from linearized versions of the full-order PDEs) into an optimal discrete-time state-space reduced-order system using the method of subspace-based realization algorithms (xRAs) [11]. Figure 2 describes the steps involved in the ROM-generation approach adopted from [10]. The "xRA" block in the diagram can be any of the family of xRA algorithms, namely, DRA, HRA, or LRA. See [11] for a complete account of the xRA approach.
The derivation of the electrochemical variable TFs follows the approach outlined in [3], which includes the effect of the particle/film interface (double-layer and constant-phase elements) and linearizes the

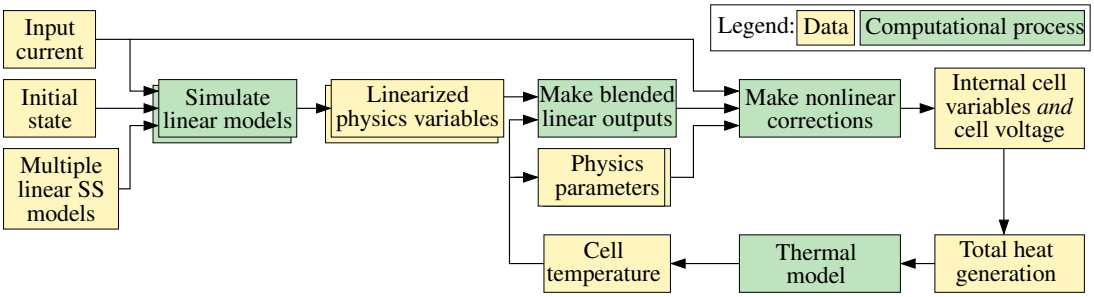

Figure 3: Time domain simulation scheme.

Butler-Volmer equation to obtain the TF of the lumped electrolyte concentration. Once, $\frac{\tilde{\Theta}_e(\tilde{x},s)}{I_{\text{app}}(s)}$ is derived, all other transfer functions may be derived from it. The TFs are then input to the xRA algorithm to generate a ROM in discrete state-space form:

$$x[k+1] = \boldsymbol{A}x[k] + \boldsymbol{B}i_{\text{app}}[k]$$
$$y[k] = \boldsymbol{C}x[k] + \boldsymbol{D}i_{\text{app}}[k].$$

A key advantage of this TF-based approach is that linear SS models can be precomputed for multiple SOC and temperature set-points for any spatial location of interest, which eliminates the need to solve for all of the variables at every spatial location. The output-blending approach [12] can then be used to simulate the cell over a wide operating range, thus accounting for the time-varying nature of the parametric battery cell model. The basic idea of the blending approach is that at every time step we generate a set of linear outputs $y_{00}[k]$, $y_{01}[k]$, $y_{10}[k]$ and $y_{11}[k]$ from the four "closest" ROMs at the present operating point (SOC,T) and then blend these four outputs using bilinear interpolation. The output-blending steps are described in detail in [12]. Next, we apply corrections to the linear outputs to account for the true nonlinear nature of the true internal cell variables, terminal voltage and total heat generation rate. The total heat generation rate is fed into the thermal model, which then calculates cell temperature and finally updates the actual temperature set-point and the temperature-dependent parameters on the subsequent time step.

3.1 Reduced-order heat generation rate modeling

Leveraging the work of Aldrich in [13], we now develop a reduced-order heat generation rate model based on the PBCET and the ROM-generation approach described previously. Note that the heat generation rate term due to polarization caused by the contact resistance q_{c} is not dependent on spatial location and cell region. As a result, we need only obtain ROMs for the other four heat generation rate terms. We start with the reversible and irreversible heat generation terms, both of which are nonlinear. We note that a ROM form can be obtained as a product of variables that have previously been realized. The ROM for the irreversible heat generation at the electrode level in the negative and positive electrodes is given by

$$q_i^{\text{r}}[\tilde{x},k] = \dot{n}^{\text{r}}[\tilde{x},k]\eta[x,k],$$

where

$$\eta^{\text{r}}[\tilde{x},k] = \frac{2RT}{F}\text{asinh}\left(\frac{\dot{n}_{\text{f}}^{\text{r}}[\tilde{x},k]}{2\dot{n}_0^{\text{r}}}\right)$$
$$= \frac{2RT}{F}\text{asinh}\left(\frac{\dot{n}_{\text{f}}^{\text{r}}[\tilde{x},k]}{2k_0^{\text{r}}\sqrt{\theta_{\text{e}}^{\text{r}}[\tilde{x},k]\left(1-\theta_{\text{ss}}^{\text{r}}[\tilde{x},k]\right)\theta_{\text{ss}}^{\text{r}}[\tilde{x},k]}}\right).$$

Similarly, for the reversible heat generation rate term, we have

$$q_{\text{r}}^{\text{r}}[\tilde{x},k] = \dot{n}^{\text{r}}[\tilde{x},k]T[k]\frac{\partial U_{\text{ocp}}(\theta_{\text{ss}}^{\text{r}}[\tilde{x},k])}{\partial T},$$

where the temperature T is updated every time step by the thermal model.

It turns out the heat generation rate terms for the Joule heating in the solid and electrolyte cannot be directly calculated from the already realized variables. Therefore, we need to derive separately TFs for the gradients $\nabla\phi_{\text{s}}$, $\nabla\phi_{\text{e}}$ and $\nabla\theta_{\text{e}}$. However, since we have already derived TFs for $\frac{\tilde{\Phi}_{\text{s}}(\tilde{x},s)}{I_{\text{app}}(s)}$, $\frac{\tilde{\Phi}_{\text{e}}(\tilde{x},s)}{I_{\text{app}}(s)}$ and $\frac{\tilde{\Theta}_{\text{e}}(\tilde{x},s)}{I_{\text{app}}(s)}$, the TFs for the gradients of those variables can be found by taking the derivative of the

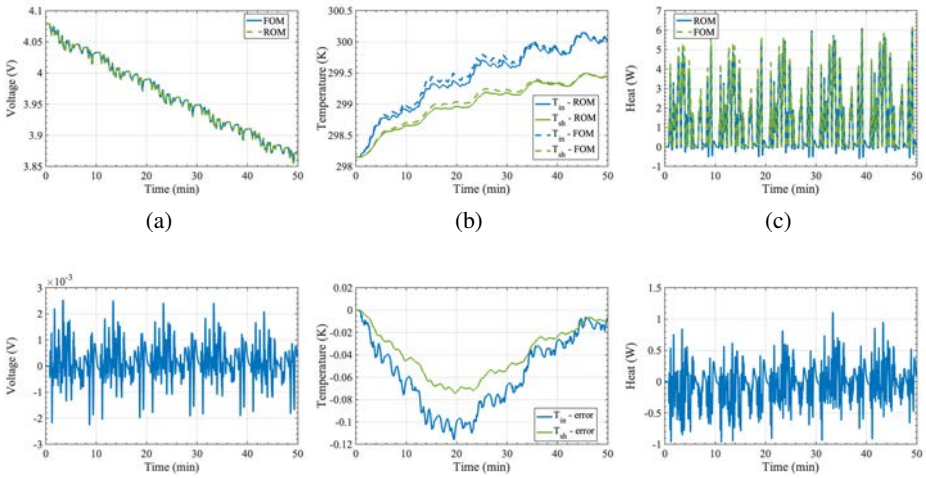

Figure 4: Comparison of time domain simulation of ROMs and FOM for a NYCC cycle profile with initial SOC of 90 %. (a) Voltage estimate. (b) Temp. estimates (c) Total heat generation rate estimate (d) Voltage estimation error (e) Temp. estimation error (f) Total heat generation rate estimation error

corresponding TFs with respect to spatial variable $\tilde{x}$. Doing so, TFs $\frac{\nabla\tilde{\Phi}_{\rm s}(\tilde{x},s)}{I_{\rm app}(s)}$, $\frac{\nabla\tilde{\Phi}_{\rm e}(\tilde{x},s)}{I_{\rm app}(s)}$ and $\frac{\nabla\tilde{\Theta}_{\rm e}(\tilde{x},s)}{I_{\rm app}(s)}$ can be used to generate the discrete-time ROMs $\nabla\tilde{\phi}_{\rm s}[\tilde{x},k]$, $\nabla\tilde{\phi}_{\rm e}[\tilde{x},k]$ and $\nabla\theta_{\rm e}[\tilde{x},k]$. Carrying out this process, the ROM for $q_{\rm s}$ at the negative and positive electrodes is written as a product of the linear outputs of $\nabla\tilde{\phi}_{\rm s}[\tilde{x},k]$, which yields

$$q_{\rm s}^{\rm r}[\tilde{x},k] = \bar{\sigma}^{\rm r}\nabla\tilde{\phi}_{\rm s}^{\rm r}[\tilde{x},k]\nabla\tilde{\phi}_{\rm s}^{\rm r}[\tilde{x},k].$$

Similarly, the ROM for $q_{\rm e}$ at the separator and negative/positive electrodes is written as a sum of the product of the linear outputs of $\nabla\tilde{\phi}_{\rm e}[\tilde{x},k]$ and $\nabla\theta_{\rm e}[\tilde{x},k]$, which yields

$$q_{\rm e}[\tilde{x},k] = \kappa_{\rm eff}\left(\nabla\phi_e[\tilde{x},k]\nabla\phi_e[\tilde{x},k]\right) + \kappa_{D,\rm eff}\left(\nabla\theta_e[\tilde{x},k]\nabla\phi_e[\tilde{x},k]\right).$$

We note that so far we have developed ROMs for the heat generation rate terms only for a given spatial location $\tilde{x}$. Therefore, in order to calculate the average heat generation rate $\bar{q}[k]$ at the separator and negative/positive electrodes we must generate ROMs at different locations within the cell and then perform integration over the respective region, which yields

$$\bar{q}_{\rm j}^{\rm r}[k] = \int_0^1 q_j[z,k]dz$$

where $\rm j \in \{i,\ r,\ e,\ s\}$; $z = \tilde{x}$ in the negative electrode; $z = \tilde{x} - 1$ in the separator region; $z = 3 - \tilde{x}$ in the positive electrode. Finally, the total heat generation rate is computed as the sum of the average heat generation rate terms at each cell region in addition to the ohmic contact resistance heat generation rate term:

$$\bar{q}[k] = \bar{q}^{\rm n}[k] + \bar{q}^{\rm s}[k] + \bar{q}^{\rm p}[k] + R_{\rm c}i_{\rm app}[k],$$

where

$$\begin{aligned}
\bar{q}^{\rm n}[k] &= \bar{q}_{\rm i}^{\rm n}[k] + \bar{q}_{\rm r}^{\rm n}[k] + \bar{q}_{\rm s}^{\rm n}[k] + \bar{q}_{\rm e}^{\rm n}[k] \\
\bar{q}^{\rm s}[k] &= \bar{q}_{\rm e}^{\rm s}[k] \\
\bar{q}^{\rm p}[k] &= \bar{q}_{\rm i}^{\rm p}[k] + \bar{q}_{\rm r}^{\rm p}[k] + \bar{q}_{\rm s}^{\rm p}[k] + \bar{q}_{\rm e}^{\rm p}[k].
\end{aligned}$$

4 Simulation results and discussion

In this section, we present time domain simulations based on the framework of Fig. 3 to demonstrate the performance of the proposed model where results are compared against a full-order model (FOM) in COMSOL. Cell parameters are for a 30Ah NMC cell adopted from [14, 15]. A set of $8^{\rm th}$-order

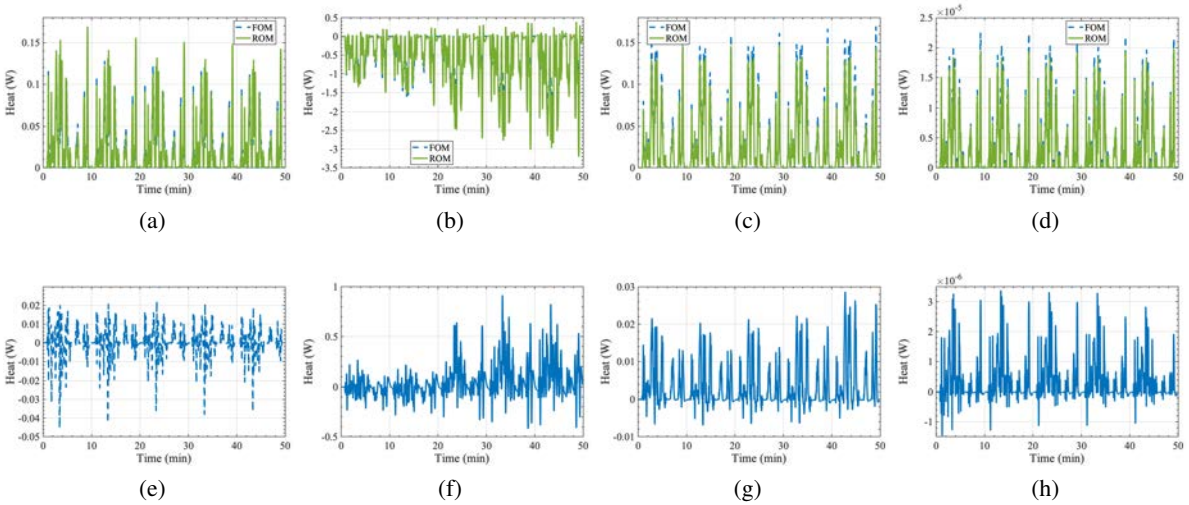

Figure 5: Average heat generation rate terms of the anode. (a) $\bar{q}_{\mathrm{i}}^{\mathrm{neg}}$ estimate. (b) $\bar{q}_{\mathrm{r}}^{\mathrm{neg}}$ estimate. (c) $\bar{q}_{e}^{\mathrm{neg}}$ estimate. (d) $\bar{q}_{\mathrm{s}}^{\mathrm{neg}}$ estimate. (e) $\bar{q}_{\mathrm{i}}^{\mathrm{neg}}$ estimation error. (f) $\bar{q}_{\mathrm{r}}^{\mathrm{neg}}$ estimation error. (g) $\bar{q}_{e}^{\mathrm{neg}}$ estimation error. (h) $\bar{q}_{\mathrm{s}}^{\mathrm{neg}}$ estimation error.

electrochemical ROMs were created at 2% SOC and 10ºC temperature intervals using the HRA algorithm [11]. Heat generation ROMs were created for the same SOC and temperature set-points at intervals of $\tilde{x} = 0.2$ within the three cell regions. Simulations employed output blending to capture time-varying behavior and used the New York city cycle (NYCC) input current profile to discharge the battery from 95% to 75% SOC. A comparison between ROM and FOM voltage, temperature and total heat generation rate and corresponding estimation errors appear in Fig. 4. Note that the total heat generation rate in Fig. 4c is the sum of the average heat generation rate terms calculated using Eq. 4c and is the input to the thermal model in Eq. 3.

A comparison between ROM and FOM for individual average heat generation rate terms and associated estimation errors in the anode and cathode appear in Figs. 5 and 6, respectively. Since the heat generation due to polarization caused by the contact resistance does not depend on any electrochemical variable or spatial location, its result is omitted here (but accounted for in the total heat generation of Fig. 4c). One can verify from Figs. 5 and 6 that q_{i}, q_{e} and q_{r} are the main contributors to temperature rise while q_{s} is comparatively small, indicating contributions from this term can be neglected.

Acknowledgments

The information, data, or work presented herein was funded in part by the National Science Foundation under award to the ASPIRE Engineering Research Center headquartered at Utah State University in Logan, UT.

Summary

State-of-the-art battery management systems (BMS) rely on highly accurate battery models for the timely parameter estimates needed during operation. A battery's thermal behavior introduces critical limits on battery performance and lifetime. This paper developed an integrated physics-based electrochemical-thermal reduced order model for lithium-ion battery cells that can be used in state estimation and advance control schemes applied to on-board BMS applications to improve battery performance and lifetime.

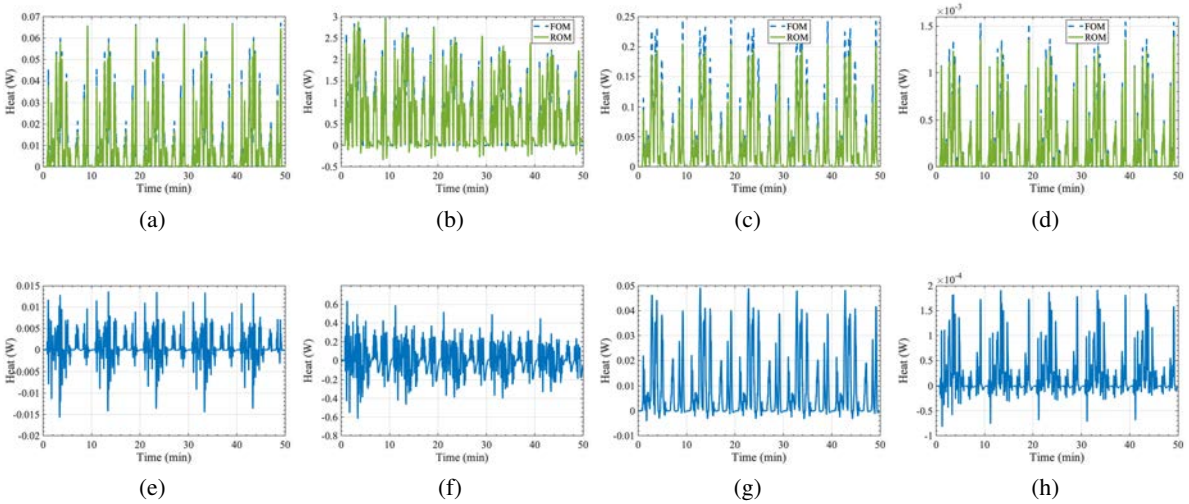

Figure 6: Average heat generation rate terms of the cathode. (a) $\bar{q}_{\mathrm{i}}^{\mathrm{pos}}$ estimate. (b) $\bar{q}_{\mathrm{r}}^{\mathrm{pos}}$ estimate. (c) $\bar{q}_{e}^{\mathrm{pos}}$ estimate. (d) $\bar{q}_{\mathrm{s}}^{\mathrm{pos}}$ estimate. (e) $\bar{q}_{\mathrm{i}}^{\mathrm{pos}}$ estimation error. (f) $\bar{q}_{\mathrm{r}}^{\mathrm{pos}}$ estimation error. (g) $\bar{q}_{e}^{\mathrm{pos}}$ estimation error. (h) $\bar{q}_{\mathrm{s}}^{\mathrm{pos}}$ estimation error.

A Deriving the gradient TFs

Gradient TF of $\ln \theta_{\mathrm{e}}$ The de-biased lumped electrolyte concentration was previously defined in [3] as $\tilde{\theta}_{\mathrm{e}}(\tilde{x},t) = \theta_{\mathrm{e}}(\tilde{x},t) - \theta_{\mathrm{e},0}(\tilde{x},t)$, where $\theta_{\mathrm{e},0}$ is the equilibrium electrolyte concentration, which is equal to 1 in the LPM. The natural logarithm of the electrolyte concentration is defined as $\ln\left(\theta_e\left(\tilde{x},s\right)\right) = \tilde{\theta}_e\left(\tilde{x},s\right)$, after forming the Taylor-series expansion of θ_{e}. In order to proceed, we must find the gradient TF of $\tilde{\theta}_{\mathrm{e}}$. The TF of the electrolyte concentration for the negative/positive electrode was derived in [3] as

$$\frac{\widetilde{\Theta}_{\mathrm{e}}^{\mathrm{r}}(\widetilde{x},s)}{I_{\mathrm{app}}(s)} = c_1^{\mathrm{r}}(s)e^{\Lambda_1^{\mathrm{r}}(s)\widetilde{x}} + c_2^{\mathrm{r}}(s)e^{-\Lambda_1^{\mathrm{r}}(s)\widetilde{x}} + c_3^{\mathrm{r}}(s)e^{\Lambda_2^{\mathrm{r}}(s)\widetilde{x}} + c_4^{\mathrm{r}}(s)e^{-\Lambda_2^{\mathrm{r}}(s)\widetilde{x}}, \tag{8}$$

where

$$\Lambda_1^{\mathrm{r}}(s) = \sqrt{\frac{1}{2}\left(\tau_1^{\mathrm{r}}(s) - \sqrt{\left(\tau_1^{\mathrm{r}}(s)\right)^2 - 4\tau_2^{\mathrm{r}}(s)}\right)} \quad \Lambda_2^{\mathrm{r}}(s) = \sqrt{\frac{1}{2}\left(\tau_1^{\mathrm{r}}(s) + \sqrt{\left(\tau_1^{\mathrm{r}}(s)\right)^2 - 4\tau_2^{\mathrm{r}}(s)}\right)}$$

$$\tau_1^{\mathrm{r}}(s) = \frac{3600\bar{q}_{\mathrm{e}}^{\mathrm{r}}s}{\bar{\psi}_{\bar{\kappa}^{\mathrm{r}}}} + \frac{1}{\bar{Z}_{\mathrm{s}}^{\mathrm{r}}(s)}\left(\frac{1}{\bar{\sigma}^{\mathrm{r}}} + \frac{1}{\bar{\kappa}^{\mathrm{r}}}\right) - \frac{\bar{\kappa}_D T}{\bar{\psi}\bar{\kappa}^{\mathrm{r}}\bar{Z}_{\widetilde{\mathrm{se}}}^{\mathrm{r}}(s)} \quad \tau_2^{\mathrm{r}}(s) = \frac{3600\bar{q}_{\mathrm{e}}^{\mathrm{r}}s}{\bar{\psi}^{\mathrm{r}}\bar{Z}_{\widetilde{\mathrm{se}}}^{\mathrm{r}}(s)}\left(\frac{1}{\bar{\sigma}^{\mathrm{r}}} + \frac{1}{\bar{\kappa}^{\mathrm{r}}}\right),$$

and where $\bar{Z}_{\widetilde{\mathrm{se}}}$ is the impedance of the solid/electrolyte interface. The TF of the electrolyte concentration in the separator was defined as

$$\frac{\widetilde{\Theta}_{\mathrm{e}}^{\mathrm{s}}(\widetilde{x},s)}{I_{\mathrm{app}}(s)} = c_1^{\mathrm{s}}(s)e^{\Lambda_1^{\mathrm{s}}(s)(\widetilde{x}-1)} + c_2^{\mathrm{s}}(s)e^{-\Lambda_1^{\mathrm{s}}(s)\widetilde{x}}. \tag{9}$$

where $\Lambda_1^{\mathrm{s}}(s) = \sqrt{\frac{3600\bar{q}_{\mathrm{e}}^{\mathrm{s}}}{\psi\bar{\kappa}^{\mathrm{s}}}s}$. Next, the TF of $\nabla\tilde{\theta}_{\mathrm{e}}$ for the negative/positives electrodes is found by taking the gradient with respect to $\tilde{x}$ of Eq. 8

$$\frac{\nabla_{\tilde{x}}\widetilde{\Theta}_{\mathrm{e}}^{\mathrm{r}}(\widetilde{x},s)}{I_{\mathrm{app}}(s)} = c_1^{\mathrm{r}}(s)\Lambda_1^{\mathrm{r}}(s)e^{\Lambda_1^{\mathrm{r}}(s)\widetilde{x}} - c_2^{\mathrm{r}}(s)\Lambda_1^{\mathrm{r}}(s)e^{-\Lambda_1^{\mathrm{r}}(s)\widetilde{x}} + c_3^{\mathrm{r}}(s)\Lambda_2^{\mathrm{r}}(s)e^{\Lambda_2^{\mathrm{r}}(s)\widetilde{x}} - c_4^{\mathrm{r}}(s)\Lambda_2^{\mathrm{r}}(s)e^{-\Lambda_2^{\mathrm{r}}(s)\widetilde{x}}.$$

For the separator, we formulate the gradient with respect to $\tilde{x}$ of Eq. 9, which yields

$$\frac{\nabla_{\tilde{x}}\widetilde{\Theta}_{\mathrm{e}}^{\mathrm{s}}(\widetilde{x},s)}{I_{\mathrm{app}}(s)} = c_1^{\mathrm{s}}(s)\Lambda_1^{\mathrm{s}}(s)e^{\Lambda_1^{\mathrm{r}}(s)\widetilde{x}} - c_2^{\mathrm{s}}(s)\Lambda_1^{\mathrm{s}}(s)e^{-\Lambda_1^{\mathrm{r}}(s)\widetilde{x}}.$$

Gradient TF of electrolyte potential $\nabla\phi_{\mathrm{e}}$ The de-biased lumped electrolyte potential was previously defined in [3] as $\tilde{\phi}_{\mathrm{e}}(\tilde{x},t) = \phi_{\mathrm{e}}(\tilde{x},t) - \phi_{\mathrm{e},0}(0,t)$. Taking the gradient yields $\nabla\tilde{\phi}_{\mathrm{e}}(\tilde{x},t) = \nabla\phi_{\mathrm{e}}(\tilde{x},t) -$

$\nabla\phi_{\mathrm{e},0}(0,t)$. However, $\nabla\phi_{\mathrm{e},0}(0,t)$ is not dependent on $\tilde{x}$; therefore, $\nabla\tilde{\phi}_{\mathrm{e}}(\tilde{x},t) = \nabla\phi_{\mathrm{e}}(\tilde{x},t)$. The electrolyte potential TF in the negative electrode was defined in [3] as

$$\frac{\widetilde{\Phi}^{\mathrm{n}}_{\mathrm{e}}(\widetilde{x},s)}{I_{\mathrm{app}}(s)} = \frac{\left[\widetilde{\Phi}^{\mathrm{n}}_{\mathrm{e}}(\widetilde{x},s)\right]_1}{I_{\mathrm{app}}(s)} + \frac{\left[\widetilde{\Phi}^{\mathrm{n}}_{\mathrm{e}}(\widetilde{x},s)\right]_2}{I_{\mathrm{app}}(s)} \tag{10}$$

where

$$\begin{aligned}\frac{\left[\widetilde{\Phi}^{\mathrm{n}}_{\mathrm{e}}(\widetilde{x},s)\right]_1}{I_{\mathrm{app}}(s)} =& -\left(\frac{\mathrm{j}^{\mathrm{n}}_1\left(e^{\Lambda^{\mathrm{n}}_1(\widetilde{x}-1)} - e^{-\Lambda^{\mathrm{n}}_1}\right) - \widetilde{x}\Lambda^{\mathrm{n}}_1 e^{-\Lambda^{\mathrm{n}}_1}\right)}{\bar{\kappa}^{\mathrm{n}}\left(\Lambda^{\mathrm{n}}_1\right)^2} + \frac{\mathrm{j}^{\mathrm{n}}_2\left(e^{-\Lambda^{\mathrm{n}}_1\widetilde{x}} - 1 + \widetilde{x}\Lambda^{\mathrm{n}}_1\right)}{\bar{\kappa}^{\mathrm{n}}\left(\Lambda^{\mathrm{n}}_1\right)^2}\right.\\ &\left. + \frac{\mathrm{j}^{\mathrm{n}}_3\left(e^{\Lambda^{\mathrm{n}}_2(\widetilde{x}-1)} - e^{-\Lambda^{\mathrm{n}}_2} - \widetilde{x}\Lambda^{\mathrm{n}}_2 e^{-\Lambda^{\mathrm{n}}_2}\right)}{\bar{\kappa}^{\mathrm{n}}\left(\Lambda^{\mathrm{n}}_2\right)^2} + \frac{\mathrm{j}^{\mathrm{n}}_4\left(e^{-\Lambda^{\mathrm{n}}_2\widetilde{x}} - 1 + \widetilde{x}\Lambda^{\mathrm{n}}_2\right)}{\bar{\kappa}^{\mathrm{n}}\left(\Lambda^{\mathrm{n}}_2\right)^2}\right),\\ \frac{\left[\widetilde{\Phi}^{\mathrm{n}}_{\mathrm{e}}(\widetilde{x},s)\right]_2}{I_{\mathrm{app}}(s)} =& -\bar{\kappa}_D T\left(c^{\mathrm{n}}_1\left(e^{\Lambda^{\mathrm{n}}_1(\widetilde{x}-1)} - e^{-\Lambda^{\mathrm{n}}_1}\right) + c^{\mathrm{n}}_2\left(e^{-\Lambda^{\mathrm{n}}_1\widetilde{x}} - 1\right)\right.\\ &\left. + c^{\mathrm{n}}_3\left(e^{\Lambda^{\mathrm{n}}_2(\widetilde{x}-1)} - e^{-\Lambda^{\mathrm{n}}_2}\right) + c^{\mathrm{n}}_4\left(e^{-\Lambda^{\mathrm{n}}_2\widetilde{x}} - 1\right)\right).\end{aligned}$$

Taking the gradient of Eq. 10 yields

$$\frac{\nabla_{\tilde{x}}\widetilde{\Phi}^{\mathrm{n}}_{\mathrm{e}}(\widetilde{x},s)}{I_{\mathrm{app}}(s)} = \frac{\left[\nabla_{\tilde{x}}\widetilde{\Phi}^{\mathrm{n}}_{\mathrm{e}}(\widetilde{x},s)\right]_1}{I_{\mathrm{app}}(s)} + \frac{\left[\nabla_{\tilde{x}}\widetilde{\Phi}^{\mathrm{n}}_{\mathrm{e}}(\widetilde{x},s)\right]_2}{I_{\mathrm{app}}(s)}$$

where

$$\begin{aligned}\frac{\left[\nabla_{\tilde{x}}\widetilde{\Phi}^{\mathrm{n}}_{\mathrm{e}}(\tilde{x},s)\right]_1}{I_{\mathrm{app}}(s)} =& -\left(\frac{\mathrm{j}^{\mathrm{n}}_1\left(e^{\Lambda^{\mathrm{n}}_1(\tilde{x}-1)} - e^{-\Lambda^{\mathrm{n}}_1}\right)}{\bar{\kappa}^{\mathrm{n}}\Lambda^{\mathrm{n}}_1} + \frac{\mathrm{j}^{\mathrm{n}}_2\left(-e^{-\Lambda^{\mathrm{n}}_1\tilde{x}} + 1\right)}{\bar{\kappa}^{\mathrm{n}}\Lambda^{\mathrm{n}}_1}\right.\\ &\left. + \frac{\mathrm{j}^{\mathrm{n}}_3\left(e^{\Lambda^{\mathrm{n}}_2(\tilde{x}-1)} - e^{-\Lambda^{\mathrm{n}}_2}\right)}{\bar{\kappa}^{\mathrm{n}}\Lambda^{\mathrm{n}}_2} + \frac{\mathrm{j}^{\mathrm{n}}_4\left(-e^{-\Lambda^{\mathrm{n}}_2\tilde{x}} + 1\right)}{\bar{\kappa}^{\mathrm{n}}\Lambda^{\mathrm{n}}_2}\right)\\ \frac{\left[\nabla_{\tilde{x}}\widetilde{\Phi}^{\mathrm{n}}_{\mathrm{e}}(\widetilde{x},s)\right]_2}{I_{\mathrm{app}}(s)} =& -\bar{\kappa}_D T\left(\Lambda^{\mathrm{n}}_1\left(c^{\mathrm{n}}_1 e^{\Lambda^{\mathrm{n}}_1(\tilde{x}-1)} - c^{\mathrm{n}}_2 e^{-\Lambda^{\mathrm{n}}_1\tilde{x}}\right) + \Lambda^{\mathrm{n}}_2\left(c^{\mathrm{n}}_3 e^{\Lambda^{\mathrm{n}}_2(\tilde{x}-1)} - c^{\mathrm{n}}_4 e^{-\Lambda^{\mathrm{n}}_2\tilde{x}}\right)\right.\end{aligned}$$

The electrolyte potential TF for the separator is defined as

$$\frac{\widetilde{\Phi}^{\mathrm{s}}_{\mathrm{e}}(\widetilde{x},s)}{I_{\mathrm{app}}(s)} = \frac{\widetilde{\Phi}^{\mathrm{n}}_{\mathrm{e}}(1,s)}{I_{\mathrm{app}}(s)} - \frac{\widetilde{x}}{\bar{\kappa}^{\mathrm{s}}} - \bar{\kappa}_D T\left(c^{\mathrm{s}}_1\left(e^{\Lambda^{\mathrm{s}}_1\widetilde{x}} - e^{-\Lambda^{\mathrm{s}}_1}\right) + c^{\mathrm{s}}_2\left(e^{-\Lambda^{\mathrm{s}}_1\widetilde{x}} - 1\right)\right).$$

and, taking the gradient yields

$$\frac{\nabla_{\tilde{x}}\widetilde{\Phi}^{\mathrm{s}}_{\mathrm{e}}(\widetilde{x},s)}{I_{\mathrm{app}}(s)} = -\frac{1}{\bar{\kappa}^{\mathrm{s}}} - \bar{\kappa}_D T\Lambda^{\mathrm{s}}_1\left(c^{\mathrm{s}}_1 e^{\Lambda^{\mathrm{s}}_1(\widetilde{x}-1)} - c^{\mathrm{s}}_2 e^{-\Lambda^{\mathrm{s}}_1(\widetilde{x}-1)}\right).$$

Finally, the electrolyte potential TF for the positive electrode is given by [3] as,

$$\frac{\widetilde{\Phi}^{\mathrm{p}}_{\mathrm{e}}(\widetilde{x},s)}{I_{\mathrm{app}}(s)} = \frac{\widetilde{\Phi}^{\mathrm{s}}_{\mathrm{e}}(1,s)}{I_{\mathrm{app}}(s)} + \frac{\left[\widetilde{\Phi}^{\mathrm{p}}_{\mathrm{e}}(\widetilde{x},s)\right]_1}{I_{\mathrm{app}}(s)} + \frac{\left[\widetilde{\Phi}^{\mathrm{p}}_{\mathrm{e}}(\widetilde{x},s)\right]_2}{I_{\mathrm{app}}(s)}$$

$$\begin{aligned}\frac{\left[\widetilde{\Phi}^{\mathrm{p}}_{\mathrm{e}}(\widetilde{x},s)\right]_1}{I_{\mathrm{app}}(s)} =& \frac{(\widetilde{x}-1)}{\bar{\kappa}^{\mathrm{p}}} - \left(\frac{\mathrm{j}^{\mathrm{p}}_1\left(e^{\Lambda^{\mathrm{p}}_1(\widetilde{x}-1)} + (1-\widetilde{x})\Lambda^{\mathrm{p}}_1 - 1\right)}{\bar{\kappa}^{\mathrm{p}}\left(\Lambda^{\mathrm{p}}_1\right)^2} + \frac{\mathrm{j}^{\mathrm{p}}_2\left(e^{-\Lambda^{\mathrm{p}}_1\widetilde{x}} + (\widetilde{x}-1)\Lambda^{\mathrm{p}}_1 e^{-\Lambda^{\mathrm{p}}_1} - e^{-\Lambda^{\mathrm{p}}_1}\right)}{\bar{\kappa}^{\mathrm{p}}\left(\Lambda^{\mathrm{p}}_1\right)^2}\right.\\ &\left. + \frac{\mathrm{j}^{\mathrm{p}}_3\left(e^{\Lambda^{\mathrm{p}}_2(\widetilde{x}-1)} + (1-\widetilde{x})\Lambda^{\mathrm{p}}_2 - 1\right)}{\bar{\kappa}^{\mathrm{p}}\left(\Lambda^{\mathrm{p}}_2\right)^2} + \frac{\mathrm{j}^{\mathrm{p}}_4\left(e^{-\Lambda^{\mathrm{p}}_2\widetilde{x}} + (\widetilde{x}-1)\Lambda^{\mathrm{p}}_2 e^{-\Lambda^{\mathrm{p}}_2} - e^{-\Lambda^{\mathrm{p}}_2}\right)}{\bar{\kappa}^{\mathrm{p}}\left(\Lambda^{\mathrm{p}}_2\right)^2}\right)\\ \frac{\left[\widetilde{\Phi}^{\mathrm{p}}_{\mathrm{e}}(\widetilde{x},s)\right]_2}{I_{\mathrm{app}}(s)} =& -\bar{\kappa}_D T\left(\Lambda^{\mathrm{P}}_1\left(c^{\mathrm{p}}_1 e^{\Lambda^{\mathrm{P}}_1(\widetilde{x}-1)} - c^{\mathrm{p}}_2 e^{-\Lambda^{\mathrm{p}}_1\widetilde{x}}\right) + \Lambda^{\mathrm{P}}_2\left(c^{\mathrm{p}}_3 e^{\Lambda^{\mathrm{P}}_2(\widetilde{x}-1)} - c^{\mathrm{p}}_4 e^{-\Lambda^{\mathrm{P}}_2\widetilde{x}}\right)\right)\end{aligned}$$

Then, the gradient TF will be

$$\frac{\nabla_{\tilde{x}}\widetilde{\Phi}_{\mathrm{e}}^{\mathrm{p}}(\widetilde{x},s)}{I_{\mathrm{app}}(s)}=\frac{\left[\nabla_{\tilde{x}}\widetilde{\Phi}_{\mathrm{e}}^{\mathrm{p}}(\widetilde{x},s)\right]_1}{I_{\mathrm{app}}(s)}+\frac{\left[\nabla_{\tilde{x}}\widetilde{\Phi}_{\mathrm{e}}^{\mathrm{p}}(\widetilde{x},s)\right]_2}{I_{\mathrm{app}}(s)},$$

where

$$\begin{aligned}\frac{\left[\nabla_{\tilde{x}}\widetilde{\Phi}_{\mathrm{e}}^{\mathrm{p}}(\widetilde{x},s)\right]_1}{I_{\mathrm{app}}(s)}=&\frac{1}{\bar{\kappa}^{\mathrm{p}}}-\left(\frac{\mathrm{j}_1^{\mathrm{p}}\left(e^{\Lambda_1^{\mathrm{p}}(\widetilde{x}-1)}-1\right)}{\bar{\kappa}^{\mathrm{p}}\Lambda_1^{\mathrm{p}}}+\frac{\mathrm{j}_2^{\mathrm{p}}\left(-e^{-\Lambda_1^{\mathrm{p}}\widetilde{x}}+e^{-\Lambda_1^{\mathrm{p}}}\right)}{\bar{\kappa}^{\mathrm{p}}\Lambda_1^{\mathrm{p}}}\right.\\&\left.+\frac{\mathrm{j}_3^{\mathrm{p}}\left(e^{\Lambda_2^{\mathrm{p}}(\widetilde{x}-1)}-1\right)}{\bar{\kappa}^{\mathrm{p}}\Lambda_2^{\mathrm{p}}}+\frac{\mathrm{j}_4^{\mathrm{p}}\left(-e^{-\Lambda_2^{\mathrm{p}}\widetilde{x}}+e^{-\Lambda_2^{\mathrm{p}}}\right)}{\bar{\kappa}^{\mathrm{p}}\Lambda_2^{\mathrm{p}}}\right),\end{aligned}$$

$$\frac{\left[\nabla_{\tilde{x}}\widetilde{\Phi}_{\mathrm{e}}^{\mathrm{p}}(\widetilde{x},s)\right]_2}{I_{\mathrm{app}}(s)}=-\bar{\kappa}_D T\left(\Lambda_1^{\mathrm{P}}\left(c_1^{\mathrm{p}}e^{\Lambda_1^{\mathrm{P}}(\widetilde{x}-1)}-c_2^{\mathrm{p}}e^{-\Lambda_1^{\mathrm{p}}\widetilde{x}}\right)+\Lambda_2^{\mathrm{P}}\left(c_3^{\mathrm{p}}e^{\Lambda_2^{\mathrm{P}}(\widetilde{x}-1)}-c_4^{\mathrm{p}}e^{-\Lambda_2^{\mathrm{P}}\widetilde{x}}\right)\right).$$

Gradient TF of solid potential The de-biased lumped solid potential was previously defined in [3] as $\tilde{\phi}_s(\widetilde{x},t)=\phi_s(\widetilde{x},t)-\phi(0,t)$. Therefore, the gradient with respect to the spatial coordinate $\widetilde{x}$ can be written as $\nabla_{\widetilde{x}}\tilde{\phi}_s(\widetilde{x},t)=\nabla_{\widetilde{x}}\phi_s(\widetilde{x},t)-\nabla_{\widetilde{x}}\phi_s(0,t)$. However, $\phi_s(0,t)$ is not a function of $\widetilde{x}$. Then, the gradient is given as $\nabla_{\widetilde{x}}\tilde{\phi}_s(\widetilde{x},t)=\nabla_{\widetilde{x}}\phi_s(\widetilde{x},t)$ and the transfer function for $\nabla_{\widetilde{x}}\tilde{\phi}_s(\widetilde{x},t)$ in the negative and positive electrode are found by taking the partial derivative with respect to $\widetilde{x}$, yielding

$$\begin{aligned}\frac{\nabla_{\widetilde{x}}\widetilde{\Phi}_{\mathrm{s}}^{\mathrm{n}}(\widetilde{x},s)}{I_{\mathrm{app}}(s)}=&-\frac{1}{\bar{\sigma}^{\mathrm{n}}}+\frac{\mathrm{j}_1^{\mathrm{n}}\left(e^{\Lambda_1^{\mathrm{n}}(\widetilde{x}-1)}-e^{-\Lambda_1^{\mathrm{n}}}\right)}{\bar{\sigma}^{\mathrm{n}}\Lambda_1^{\mathrm{n}}}+\frac{\mathrm{j}_2^{\mathrm{n}}\left(1-e^{-\Lambda_1^{\mathrm{n}}\widetilde{x}}\right)}{\bar{\sigma}^{\mathrm{n}}\Lambda_1^{\mathrm{n}}}\\&+\frac{\mathrm{j}_3^{\mathrm{n}}\left(e^{\Lambda_2^{\mathrm{n}}(\widetilde{x}-1)}-e^{-\Lambda_2^{\mathrm{n}}}\right)}{\bar{\sigma}^{\mathrm{n}}\Lambda_2^{\mathrm{n}}}+\frac{\mathrm{j}_4^{\mathrm{n}}\left(1-e^{-\Lambda_2^{\mathrm{n}}\widetilde{x}}\right)}{\bar{\sigma}^{\mathrm{n}}\Lambda_2^{\mathrm{n}}}\\\frac{\nabla_{\widetilde{x}}\widetilde{\Phi}_{\mathrm{s}}^{\mathrm{p}}(\widetilde{x},s)}{I_{\mathrm{app}}(s)}=&\frac{1}{\bar{\sigma}^{\mathrm{p}}}+\frac{\mathrm{j}_1^{\mathrm{p}}\left(e^{\Lambda_1^{\mathrm{P}}(\widetilde{x}-1)}-e^{-\Lambda_1^{\mathrm{p}}}\right)}{\bar{\sigma}^{\mathrm{p}}\Lambda_1^{\mathrm{p}}}+\frac{\mathrm{j}_2^{\mathrm{p}}\left(1-e^{-\Lambda_1^{\mathrm{P}}\widetilde{x}}\right)}{\bar{\sigma}^{\mathrm{p}}\Lambda_1^{\mathrm{p}}}\\&+\frac{\mathrm{j}_3^{\mathrm{p}}\left(e^{\Lambda_2^{\mathrm{P}}(\widetilde{x}-1)}-e^{-\Lambda_2^{\mathrm{p}}}\right)}{\bar{\sigma}^{\mathrm{p}}\Lambda_2^{\mathrm{p}}}+\frac{\mathrm{j}_4^{\mathrm{p}}\left(1-e^{-\Lambda_2^{\mathrm{P}}\widetilde{x}}\right)}{\bar{\sigma}^{\mathrm{p}}\Lambda_2^{\mathrm{p}}}\end{aligned}$$

References

[1] M. Doyle, T. F. Fuller, and J. Newman, "Modeling of galvanostatic charge and discharge of the lithium/polymer/insertion cell," *Journal of The Electrochemical Society*, vol. 140, no. 6, pp. 1526–1533, jun 1993.

[2] G. L. Plett, *Battery Management Systems, Volume I: Battery Modeling*, 1st ed. Artech House, 2015, vol. 1.

[3] Z. Chu, G. L. Plett, M. S. Trimboli, and M. Ouyang, "A control-oriented electrochemical model for lithium-ion battery, part i: Lumped-parameter reduced-order model with constant phase element," *Journal of Energy Storage*, vol. 25, p. 100828, 2019.

[4] R. Jobman, M. S. Trimboli, and G. L. Plett, "Identification of lithium-ion physics-based model parameter values," *Journal of Energy Challenges and Mechanics*, vol. 2, no. 2, pp. 45–55, 2015.

[5] T. F. Fuller, M. Doyle, and J. Newman, "Simulation and optimization of the dual lithium ion insertion cell," *Journal of The Electrochemical Society*, vol. 141, no. 1, pp. 1–10, jan 1994.

[6] M. S. T. Gregory L. Plett, "Process for lumping parameters to enable nondestructive parameter estimation for lithium-ion physics-based models," *35th International Electric Vehicle Symposium and Exhibition*, June 2022.

[7] C. Zhang, K. Li, and J. Deng, "Real-time estimation of battery internal temperature based on a simplified thermoelectric model," *Journal of Power Sources*, vol. 302, pp. 146–154, 2016.

[8] W. B. Gu and C. Wang, "Thermal-electrochemical modeling of battery systems," *Journal of the Electrochemical Society*, vol. 147, no. 8, pp. 2910–2922, 2000.

[9] A. Bizeray, S. Zhao, S. Duncan, and D. Howey, "Lithium-ion battery thermal-electrochemical model-based state estimation using orthogonal collocation and a modified extended kalman filter," *Journal of Power Sources*, vol. 296, pp. 400–412, 2015.

[10] J. L. Lee, A. Chemistruck, and G. L. Plett, "Discrete-time realization of transcendental impedance models, with application to modeling spherical solid diffusion," *Journal of Power Sources*, vol. 206, pp. 367–377, 2012.

[11] A. Rodríguez, G. L. Plett, and M. S. Trimboli, "Comparing four model-order reduction techniques, applied to lithium-ion battery-cell internal electrochemical transfer functions," *eTransportation*, vol. 1, p. 100009, 2019.

[12] A. Rodríguez Marco, "Improvements to fidelity, generation and implementation of physics-based lithium-ion reduced-order models," Ph.D. dissertation, University of Colorado Colorado Springs, 2017.

[13] M. Aldrich, "Reduced-order coupled electrochemical-thermal modeling of lithium-ion battery cells," Master's thesis, University of Colorado at Colorado Springs, 2015.

[14] J. Schmalstieg, C. Rahe, M. Ecker, and D. U. Sauer, "Full cell parameterization of a high-power lithium-ion battery for a physico-chemical model: Part i. physical and electrochemical parameters," vol. 165, no. 16, pp. A3799–A3810, 2018.

[15] J. Schmalstieg and D. U. Sauer, "Full cell parameterization of a high-power lithium-ion battery for a physico-chemical model: Part II. thermal parameters and validation," vol. 165, no. 16, pp. A3811–A3819, 2018.

Authors

Aloisio Kawakita de Souza received his M.S. degree in Electrical Engineering with an option in Battery Controls from the University of Colorado Colorado Springs where he is currently a Ph.D. candidate in Electrical Engineering. He is also a Graduate Research Assistant with the Department of Electrical and Computer Engineering where he conducts both theoretical and experimental sponsored research on advanced modeling and control methods. His research interests include modeling, system identification, state estimation, and advanced control methods applied to lithium-ion batteries for automotive applications.

Dr. Plett received his Ph.D. in Electrical Engineering from Stanford University and is now Professor of Electrical and Computer Engineering at the University of Colorado Colorado Springs. His research focuses on topics in control systems as applied to the management of high-capacity battery systems, such as found in electric vehicles. Current research efforts include: physics-based reduced-order modeling of ideal lithium-ion dynamics and degradation mechanisms; nondestructive parameter estimation for physics-based models; estimation of cell electrochemical and degradation state; state-of-charge and state-of-health estimation; life-extending power-prediction methods.

Dr. Trimboli received his Ph.D. in Control Engineering from Oxford University and is now Associate Professor of Electrical and Computer Engineering at the University of Colorado Colorado Springs. His research focuses on topics in control systems as applied to the management of high-performance battery systems. Current research efforts include: physics-based reduced-order modeling of ideal lithium-ion dynamics; MPC for battery fast-charge and power limit estimation for life extension; battery state estimation using Kalman filters; life-extending power-prediction methods.